Electrochimica Acta 269 (2018) 441e451

Contents lists available at ScienceDirect

Electrochimica Acta

journal homepage: www.elsevier.com/locate/electacta

Direct growth of ultrasmall bimetallic AuPd nanoparticles supported on nitrided carbon towards ethanol electrooxidation

Yue Yang [a, b], Lei Jin [b], Ben Liu [b], Peter Kerns [b], Jie He [b, c, *]

[a] Department of Chemical Engineering, Nanjing University of Science and Technology, Jiangsu 210094, China
[b] Department of Chemistry, University of Connecticut, Storrs, CT 06269, USA
[c] Institute of Materials Science, University of Connecticut, Storrs, CT 06269, USA

a r t i c l e i n f o

Article history:
Received 14 December 2017
Received in revised form
1 March 2018
Accepted 3 March 2018
Available online 7 March 2018

Keywords:
Bimetallic nanoparticles
Ultrasmall metal nanocatalysts
Surface ligands
Nitrided carbon
Ethanol electrooxidation

a b s t r a c t

Bimetallic nanoparticles (NPs) show interesting synergy to enhance the activity and durability in electrocatalytic alcohol oxidation compared to single-component metal NPs. The synthesis of bimetallic NPs often carried out in solution brings challenges in separating, loading and dispersing these NPs on conductive carbon supports. We herein report the direct growth of well-defined AuPd bimetallic NPs in the size range of 2e5 nm on nitrided carbon support. Our method is based on a seed-mediated growth method using Au seeds (1.8 ± 0.3 nm) supported on nitrided carbon. We show that the sizes and surface compositions of bimetallic NPs are precisely controllable. The resultant core-shell AuPd bimetallic NPs are thermally stable and they can be converted to alloyed AuPd NPs when subjected to thermal activation at 250 °C for 1 h. The chemical compositions of the AuPd alloyed NPs have been investigated by combining electron microscopy dispersive X-ray analysis, X-ray photoelectron spectroscopy and surface oxygen desorption using electrochemical reduction of catalysts. The catalytic activity, stability, poisoning tolerance and charge transfer resistance of AuPd alloyed NPs for the ethanol electrooxidation are largely enhanced compared to single-component NPs. $Au_{0.45}Pd_{0.55}$-5 nm exhibited the superior specific activity of 1.11 mA/cm^2 and mass activity of >0.4 A/mg$_{metal}$ toward ethanol oxidation, approximately 5 times more active than commercial Pd/C. We expect that this synthetic method will be of interest to prepare metallic electrocatalysts having defined nanostructures and compositions directly on conductive carbon for applications in fuel cells and batteries.

1. Introduction

Direct alcohol fuel cells (DAFCs) using liquid fuels such as methanol, ethanol and glycerol are of interest for power applications. These are superior over analogous devices that are fed with gaseous fuels such as hydrogen and natural gas, due to the high volumetric energy density and transportation portability [1e3]. Among those possible fuels, less-toxic ethanol stands out as an alternative fuel source which can be produced in large quantities from renewable resources. Nevertheless, the direct ethanol fuel cells suffer some drawbacks [4e6], e.g. sluggish anodic kinetic of ethanol electrooxidation and accumulation of poisonous intermediates, similar to other common DAFCs. Pt catalysts have been widely used as the electrocatalysts for the alcohol oxidation due to their high electrocatalytic activity. However, the high cost and the susceptibility to CO poisoning are major problems for DAFCs using Pt catalysts [7]. The incorporation of the second metals into Pt, like PtNi [8], PtCo [9], PtFe [10,11], PtSn [12], PtRu [13] and PtAu [14], can lower the overall cost of the electrocatalysts and enhance the resistance to poisonous CO while simultaneously maintaining the substantial activity. In addition, Pd-containing catalysts have been emerged as alternative "Pt-free" electrocatalysts for DAFCs since Pd has Pt-like activity and it is less expensive [15]. Bimetallic NPs with core-shell [16], dendritic [17], Janus-type [18] and intermetallic or alloyed [19] nanostructures show tunable activity, selectivity and durability in electrocatalytic alcohol oxidation [20]. When alloyed with Au, which displays high resistance for CO adsorption, AuPd bimetallic nanoparticles (NPs) are one of the more promising candidates as anodic electrocatalysts for DAFCs [21e25]. For example, Liu et al. reported that the doping of Au to Pd NPs enhanced the electrocatalytic activity for DAFCs and the mass-

* Corresponding author. Department of Chemistry, University of Connecticut, Storrs, CT 06269, USA.
E-mail address: jie.he@uconn.edu (J. He).

https://doi.org/10.1016/j.electacta.2018.03.017
0013-4686/

specific activity of $Pd_{1.0}Au/C$ (1.0 refers to the atomic ratio of Pd/Au) reached 2.3 times higher than that of Pd/C catalysts [22].

Although there is a large number of examples in the literature on the synthesis of Pd-containing bimetallic NPs through co-reduction and thermal decomposition in solution [26,27], the use of those bimetallic NPs as electrocatalysts for DAFCs requires the support of them on conductive carbon. Loading pre-synthesized NPs on conductive carbon supports often causes the aggregation of NPs. On one hand, the interaction between pre-synthesized NPs and the carbon support is weak. The physical mixing usually does not provide any control on the distribution of NPs on the support. Small NPs with high surface energy tend to aggregate instead of well dispersion on carbon supports. On the other hand, the removal of surface ligands that are commonly used to control the sizes and shapes of NPs potentially leads to the sintering and restructuring of NPs, in particular under high temperature [28]. All of those will result in the loss of active surface area or complete deactivation of the nanocatalysts.

We recently reported the synthesis of ultrasmall noble metal nanocatalysts (<2 nm, e.g., Au, Pt and Pd) directly on nitrided carbon [29]. When doping activated carbon with nitrogen through "soft" nitriding, the strong metal-carbon interaction can stabilize the nanocatalysts and prevent the overgrowth of the nanocatalysts during synthesis. We herein further extend this synthetic strategy to prepare AuPd bimetallic NPs supported on nitrided carbon. Through a facile seeded-growth on ultrasmall Au seeds, AuPd bimetallic NPs with precisely controllable sizes (monodispersed, 2-5 nm) and chemical compositions could be synthesized. The mass loading of bimetallic NPs on carbon supports reached 40 wt% without any aggregation or overgrowth. The grown AuPd bimetallic NPs are thermally stable on the carbon even when subjected to thermal activation at 250 °C for 1 h. The electrocatalytic performances of AuPd bimetallic NPs were investigated for ethanol oxidation. The alloying of bimetallic NPs showed significant enhancement of the catalytic activity, stability and CO tolerance all of which are highly desired as anodic catalysts in DAFCs.

2. Experimental

2.1. Chemicals and materials

Gold (III) chloride trihydrate ($HAuCl_4\$3H_2O$, 99.999%), sodium tetrachloropalladate (II) (Na_2PdCl_4, 99.999%), 4-mercaptobenzoic acid (4-MBA), L-ascorbic acid (AA, >99%), urea, ethanol, sodium hydroxide (NaOH), sodium borohydride ($NaBH_4$, >99%) were purchased from Sigma-Aldrich and used as received. Printex U activated carbon (AC) was kindly provided by Orion Co. Deionized water (High-Q, Inc. 103 S Stills) with a resistivity of >10.0 MU was used in all experiments.

2.2. Synthesis of Au seeds on nitrided carbon

We used Au nanoclusters (AuNCs) supported on nitrided carbon (Au-2@NC) as seeds for the further growth of bimetallic NPs. AuNCs were grown in situ using $NaBH_4$ as the reducing agent and nitrided carbon as the support by following our previous report [29]. The soft nitriding of Printex U carbon was carried out by annealing Printex U carbon with urea at 300 °C. After thoroughly washing with water and ethanol, nitrided Printex U carbon was used for all experiments throughout. In a typical experiment to grow AuNCs, 100 mg of nitrided carbon was dispersed in 200 mL of water, and sonicated for 30 min. 0.5 mL of $HAuCl_4$ aqueous solution (10 mg/mL) was then added. After sonicating for 1 h, 6 mL of ice-cooled and freshly prepared $NaBH_4$ solution (1 mg/mL) was quickly injected. The solution was stirred for another 2 h. The product was collected by centrifugation and further washed with water and ethanol. The obtained powder was dried for overnight under vacuum at 40 °C.

2.3. Synthesis of AuPd bimetallic NPs on nitrided carbon

AuPd bimetallic NPs on nitrided carbon (Au_xPd_{1-x}@NC) were prepared using a seed-mediated growth method [30]. The resultant Au-2@NC (1.8 ± 0.3 nm) were used as seeds. In a typical synthesis of $Au_{0.45}Pd_{0.55}$-5@NC, with a feeding molar ratio of Au: Pd ¼ 50: 50, 5 mg of Au-2@NC powder was dispersed in an ethanol/water solution (10 mL, 3:1 v/v) containing 4-MBA (0.4 mg, 0.275 mM), $HAuCl_4\$3H_2O$ (1.5 mg, 0.382 mM) and Na_2PdCl_4 (1.3 mg, 0.442 mM). The mixture was stirred for 10 min before the addition of AA solution (0.488 mL, 42 mM), followed by gentle stirring for 5 min. The solution was left undisturbed for overnight until the product finally precipitated with a clear supernatant. The product was centrifuged and washed with ethanol three times (5000 rpm, 10 min). The final product was dried under vacuum at 40 °C. Other bimetallic NPs were prepared using the same procedure except the different amounts and ratios of the precursors. The details of feeding ratios for Au_xPd_{1-x}@NC having different chemical composition are summarized in Table 1. We also prepared Au_xPd_{1-x}@NC having varied sizes by tuning the ratios of Au-2@NC seeds and the amount of the two precursors.

To remove surface ligands and improve the alloying of bimetallic AuPd NPs, we also carried out a thermal treatment by annealing the catalysts [28,31,32]. The collected Au_xPd_{1-x}@NC powder was heated in a tube furnace and calcined at 250 °C for 1 h under air with a heating rate of 10 °C /min. The sizes of bimetallic AuPd NPs before and after the thermal treatment were not varied as confirmed using electron microscopy as shown in Fig. 4.

2.4. Characterizations

Transmission electron microscopy (TEM) was carried out using a Thermo Fisher Scientific Tecnai T12 S/TEM with an accelerating voltage of 120 kV. High-angle annular dark-field scanning TEM (HAADF-STEM) and STEM mapping were performed using a Talos F200X Atomic Resolution Analytical Microscope. TEM samples were prepared by casting the suspension of materials on a carbon coated copper grid (400 mesh). The wide-angle XRD patterns over a 2q range of 20e85° with a continuous scan rate of 0.5°/min were obtained using a Rigaku Ultima IV diffractometer (Cu Ka radiation, l ¼ 1.5406 Å) with an operating voltage of 40 kV and a current of 44 mA. Scanning electron microscopy (SEM) was performed using an FEI Nova NanoSEM 450 with an accelerating voltage of 10 kV and a beam current of 10 mA. SEM samples were prepared by casting a suspension of the materials on silicon wafers. X-ray photoelectron spectroscopy (XPS) characterization of the synthesized materials was conducted on a PHI model Quantum 2000 spectrometer with scanning ESCA multiprobe (ϕ Physical Electronics Industries Inc.) using Al Ka radiation (l ¼ 1486.6 eV) as the radiation source. The spectra were recorded in the fixed analyzer transmission mode with pass energies of 187.85 eV and 29.35 eV for recording survey and high resolution spectra, respectively. The powder samples were pressed on a double sided carbon tape mounted on an Al coupon pinned to a sample stage with a washer and screw then placed in the analysis chamber. Binding energies (BE) were measured for Pd 3 d, Au 4f, N 1s, C 1s and O 1s. The obtained XPS spectra were analyzed and fitted using CasaXPS software (version 2.3.16). Sample charging effects were eliminated by correcting the observed spectra with the C 1s BE value of 284.8 eV.

Table 1
Summary for atomic compositions of Au_xPd_{1-x}@NC calculated by different methods.

Sample No.	Sample	Feeding ratio		EDX-mapping		XPS		Electrochemistry	
		Au (at %)	Pd (at %)	Au (at %)	Pd (at %)	Au (at %)	Pd (at %)	Au (at %)	Pd (at %)
1	Au-5@NC	100	0	100	0	100	0	100	0
2	$Au_{0.91}Pd_{0.09}$-5@NC	90	10	90.6	9.4	92.3	7.7	88.1	11.9
3	$Au_{0.82}Pd_{0.18}$-5@NC	75	25	81.9	18.1	73.5	26.5	77.5	22.5
4	$Au_{0.45}Pd_{0.55}$-5@NC	50	50	45.0	55.0	45.1	54.9	53.8	46.2
5	$Au_{0.26}Pd_{0.74}$-5@NC	25	75	26.2	73.8	e	e	17.6	82.4
6	$Au_{0.12}Pd_{0.88}$-5@NC	10	90	11.7	88.3	e	e	8.5	91.5
7	$Au_{0.07}Pd_{0.93}$-5@NC	7	93	7.5	92.5	7.5	92.5	2.9	97.1
8	$Au_{0.70}Pd_{0.30}$-2.5@NC	50	50	e	e	e	e	69.7	30.3
9	$Au_{0.57}Pd_{0.43}$-3.5@NC	50	50	e	e	e	e	56.7	43.3

2.5. Electrochemical measurement

A CHI 600 E electrochemical potentiostat (CH Instruments) was used for all electrochemical measurements. All measurements were carried out using a three-electrode cell with the saturated calomel electrode (SCE) as the reference electrode, a platinum wire as the counter electrode, and a coated pyrolytic graphite (PG) as the working electrode. The working electrode was fabricated by casting the catalyst ink on the PG electrode. Typically, 2 mg of the catalyst was dispersed in 475 mL of water/EtOH (4:1 v/v) by sonication for 30 min in a 1.5 mL testing tube. Then, 25 mL of nafion solution was added and further sonicated for another 20 min. 10 mL of the catalyst ink was dropped on the PG electrode and dried overnight before use. The electrochemical measurements were performed in N_2-saturated 1 M NaOH solution with ethanol at a scan rate of 20 mV/s at room temperature. The electrolyte was purged with high-purity N_2 for 20 min before all electrochemical measurements and with a N_2 flow on the top of the solution during the measurement. The electrochemical active surface area (ECSA) of the catalysts was estimated from surface desorption of a monolayer of oxygen on the Au-Pd surface. The coulombic charge for oxygen desorption on the pure Au and Pd are 400 mC/cm^2 and 424 mC/cm^2, respectively, as reported in literature [33]. Chronoamperometry test was operated in an N_2-saturated 1 M NaOH containing 0.6 M ethanol solution for 1200 s at the peak potential for each catalyst obtained from cyclic voltammetry (CV) measurements.

For the CO stripping voltammetry, the working electrode was immersed in 0.5 M H_2SO_4 solution (50 mL) and the solution was purged with CO for 20 min at room temperature to allow the complete adsorption of CO onto the surface of the catalyst at a fixed potential of 0.15 V vs SCE. The electrode was quickly moved to a fresh solution of N_2-purged 0.5 M H_2SO_4 for CO stripping voltammetry measurement. The CO stripping voltammetry was recorded at a sweep rate of 50 mV/s in the potential window of 0e1.3 V vs SCE.

3. Results and discussion

The soft nitriding can functionalize the carbon support with abundant surface N sites which potentially interact with and stabilize metal nanoclusters as described in our previous report [29,34]. Nitrided carbon can be used as a support to grow AuNCs through chemical reduction using $NaBH_4$ as a reductant. The growth of AuNCs on nitrided carbon was first revealed by electron microscopy (Fig. 1aec). AuNCs are well-distributed on the nitrided carbon support. The resultant AuNCs are highly monodispersed with an average diameter of 1.8 ± 0.3 nm (denoted as Au-2@NC). Au-2@NC was used as seeds for the further growth of bimetallic NPs. To stabilize larger core-shell bimetallic NPs, 4-MBA was chosen as surface ligand to assist the further growth of the outer shell in the presence of AA as the reductant. We first examined the growth of pure Au and Pd as the shell on Au-2@NC. When using $HAuCl_4$ or Na_2PdCl_4 solely as the precursor in the second growth, the shell can uniformly grow on Au seeds. The resultant spherical core-shell NPs of Au@Au-5 and Au@Pd-5 before calcination were characterized as shown in Fig. 1dei. Both core-shell NPs are well-dispersed on the carbon support as verified from TEM images. Both Au- and Pd-shell NPs have an average size of ca. 5 nm, corresponding to the shell thickness of 1.5e1.6 nm. No small Au seeds are seen under TEM, suggesting that the shell is grown uniformly. The loading amount of the core-shell NPs on carbon reached 40 wt% without any aggregation.

By varying the feeding molar ratios of the two precursors ($HAuCl_4$ and Na_2PdCl_4), the shell compositions (or the compositions of bimetallic NPs) can be readily tuned as bimetallic AuPd (Fig. S1). Fig. 2 shows representative TEM images of Au_xPd_{1-x}@NC with different varied sizes of 2.5 nm, 3.5 nm and 5 nm. Note that, the ratios in bimetallic NPs after calcination (denoted as Au_xPd_{1-x}) reported here are from SEM energy-dispersive X-ray (EDX) spectroscopy (SEM-EDX) results since the overall amount of Au_xPd_{1-x}@NC includes the contribution of Au seeds as well. The growth of the bimetallic shell shows similar uniformity as pure Au and Pd shells on Au-2@NC. Those results confirm that the sizes and compositions of NPs are precisely controllable by varying the feeding amounts and ratios of metal precursors. We synthesized several AuPd bimetallic NPs on nitrided carbon as summarized in Table 1. The compositions and the loading amount of AuPd bimetallic NPs were measured by SEM-EDX and X-ray photoelectron spectroscopy (XPS), both of which are in good consistence with the feeding ratio of the two precursors (see Table 1).

The crystallinity and the formation of AuPd bimetallic shells were further examined by powder X-ray diffraction (XRD) (Fig. 3a). Since NPs smaller than 3 nm do not show XRD peaks, XRD of Au_xPd_{1-x}-5@NC having 5 nm in diameter and different ratios of Au/Pd was collected. For Au-5@NC (pure Au grown on Au seeds), four typical broad diffraction peaks located on 38.2°, 44.3°, 64.8° and 77.8° can be indexed to the (111), (200), (220) and (311) planes of fcc metallic Au (Fig. 3a, curve 1). With adding Pd to Au, the diffraction peaks of binary AuPd NPs exhibit a gradual shift to higher 2θ values. We plotted 2θ of the (111) facet against the mole fraction of Pd in bimetallic NPs. A linear correlation showed the increase of 2θ when increasing the content of Pd (Fig. 3b). This further confirms the formation of AuPd alloy according to the Vegard's law [35,36].

In our previous studies, we showed that the use of organic surface ligands potentially blocked surface active sites and slowed down the electron transfer [31,37]. Therefore, the removal of surface ligands is necessary before electrochemical measurements. High-temperature calcination at 250 °C in air was used to remove 4-MBA ligands. To confirm the removal of 4-MBA ligands, the

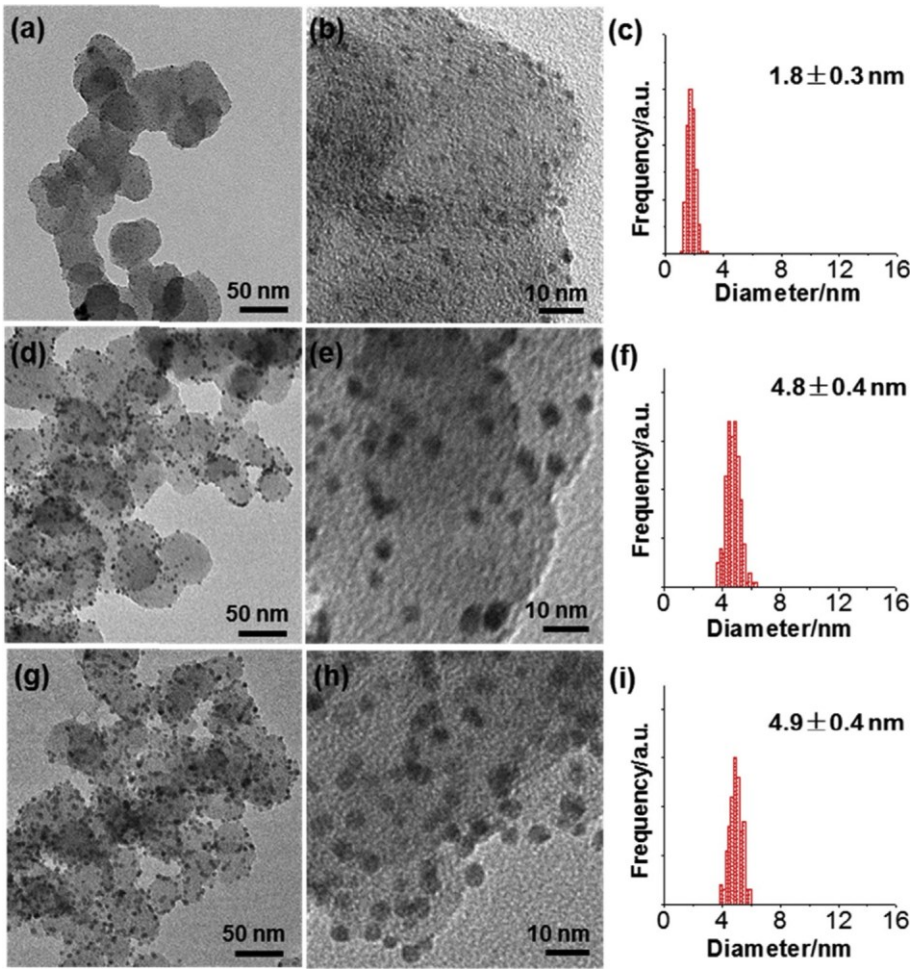

Fig. 1. Representative TEM images and the corresponding size distribution histograms of Au-2@NC (aec), Au@Au-5@NC (def) and Au@Pd-5@NC (gei).

catalytic activity of representative nanocatalysts Au-5@NC, $Au_{0.45}Pd_{0.55}$-5@NC and $Au_{0.07}Pd_{0.93}$-5@NC before and after calcination were compared using cyclic voltammetry (CV) measurements for ethanol oxidation in N_2 saturated 1 M NaOH containing 0.6 M ethanol (Figure S2a-c). For Au-5@NC before calcination, the anodic oxidation peak is around 0.13 V (vs. SCE, all potentials reported is relative to SCE) with a peak current of 0.075 A/mg_{Au}. The removal of surface ligands resulted in the lowering of the oxidation peak potential ca. 20 mV after calcination and the increase of the peak current to 0.18 A/mg_{Au} and 0.54 A/mg_{AuPd} for Au-5@NC and $Au_{0.45}Pd_{0.55}$-5@NC, respectively (Fig. S2d). This result, similar to what we observed in Au-2@NC, is likely due to the removal of electron transfer barriers between catalysts and reactants [29,38]. In contrast, the peak potential of $Au_{0.07}Pd_{0.93}$-5@NC shifted from −0.27 V to −0.23 V after calcination, although the increase in current density was apparent (Fig. S2c). This is presumably because of the diffusion of Au from the core to the surface of NPs during the calcination.

The surface composition variation of the two components on the surfaces during the calcination was investigated using CV in 1 M NaOH at a scan rate of 50 mV/s in the potential range from −0.8 to 0.5 V (Fig. 4 and Figs S3-4). In the absence of ethanol, the oxidation (or reduction) of the catalysts is a powerful method to analyze the surface compositions. For example, an evident reduction peak of the oxygen desorption peak at 0.02 V exhibited in the cathodic scan for the Au-5@NC (Fig. 4, curve 1). While for the series of AuPd bimetallic NPs, two distinguishable peaks were observed when the fraction of Pd is less than 50%. The dominant cathodic peak at approximately 0.02 V can be ascribed to the reduction of gold oxides when compared with that of pure Au(0). The other peak at around −0.25 V for $Au_{0.91}Pd_{0.09}$-5@NC (Fig. 4, curve 2) and $Au_{0.82}Pd_{0.18}$-5@NC (Fig. 4, curve 3) is attributed to the reduction of AuPd alloy domain as reported by Jirkovsk et al. [35]. This suggests the surface phase segregation of Au-Pd domains on an Au-rich surface. When comparing the CV of $Au_{0.45}Pd_{0.55}$-5@NC before calcination (Fig. S4), three distinguishable peaks at −0.45 V, −0.26 V and 0.02 V were observed in the cathodic scan. Those peaks are attributed to the oxygen desorption of Pd, AuPd alloy and Au respectively. Merging of the three peaks at lower potentials for the calcined $Au_{0.45}Pd_{0.55}$-5@NC is indicative of "realloying" during calcination where the surface of bimetallic NPs became more homogenous. This result further supports the increase in the oxidation potential of $Au_{0.45}Pd_{0.55}$-5@NC after the removal of surface ligands as described above. In addition, a gradual negative shift on the oxygen desorption peak potential of alloyed AuPd from −0.24 V for $Au_{0.91}Pd_{0.09}$-5@NC to −0.46 V for $Au_{0.07}Pd_{0.93}$-5@NC was seen with increasing Pd content in NPs. This reveals the potential of the reduction of bimetallic NPs is proportional to the composition as shown in Fig. 4b [33,39,40]. The calculated mole fractions from the electro characterization of the two metals is also listed in Table 1. Those values are relatively close to the XPS and SEM-EDX results (see below).

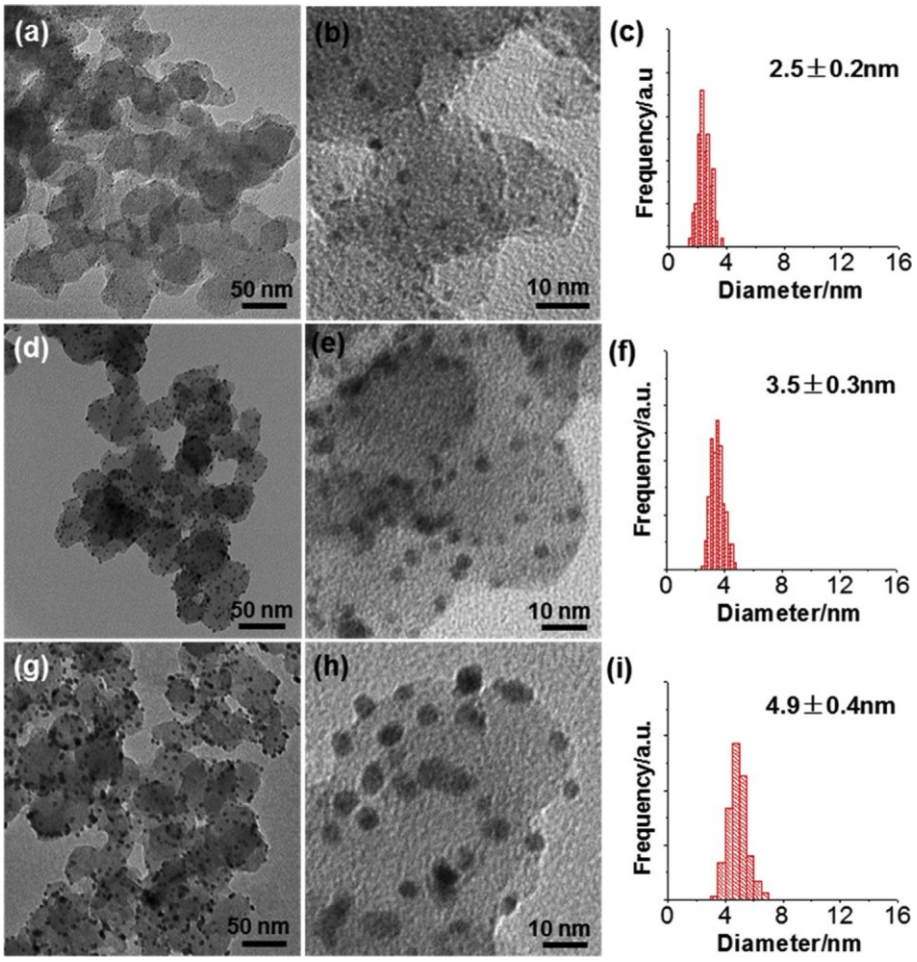

Fig. 2. Representative TEM images and corresponding size distribution histograms of $Au_{0.70}Pd_{0.30}$-2.5@NC (aec), $Au_{0.57}Pd_{0.43}$-3.5@NC (def), and $Au_{0.45}Pd_{0.55}$-5@NC (gei).

The electrochemical active surface areas (ECSAs) of the catalysts were further estimated from surface reduction of those catalysts, by the equation (see Table 2), ECSA ¼ Q_o/q_o, where Q_o is the surface charge that can be obtained from the area under the CV trace of oxygen desorption and q_o is the charge required for desorption of a monolayer of oxygen on the Au-Pd surface. q_o was calculated using q_0 ¼ q_{Au}* m_{Au} þ q_{Pd}* m_{Pd}, where q_{Au} and q_{Pd} are the coulombic charge for the oxygen desorption on pure Au and Pd, and m_{Au} and m_{Pd} are the mole fraction of Au and Pd (%), respectively [33,39].

XPS was carried out to confirm the compositions and chemical states of Au and Pd in bimetallic NPs. All samples for XPS studies were calcined to remove the surface ligands. The XPS survey spectra are given in Fig. 5, showing the absence of S element in the NPs and further confirming the complete removal of the ligands. The chemical compositions of NPs can be estimated from Au 4f and Pd 3 d peaks as summarized in Table 1. The compositions of bimetallic NPs are consistent with SEM-EDX results (see Table 1). The high resolution Au 4f peaks and Pd 3 d peaks suggest the different oxidation states of Au and Pd with different compositions. Pure Au-5@NC show Au $4f_{7/2}$ and Au $4f_{5/2}$ binding energies at 84.3 and 88.0 eV (Fig. 5b), respectively. A gradual decrease in Au 4f binding energy was observed when alloying with Pd. For example, Au $4f_{7/2}$ shifted to 84.2 eV for $Au_{0.91}Pd_{0.09}$-5@NC, 84.1 eV for $Au_{0.45}Pd_{0.55}$-5@NC and 84.0 eV for $Au_{0.07}Pd_{0.93}$-5@NC. On the other hand, Pd $3d_{3/2}$ peaks shift to slight higher binding energy when increasing the Pd amount in bimetallic NPs (Fig. 5c). In case of Pd $3d_{3/2}$ peaks, a large hump at 337.5 eV was found in all bimetallic samples and this hump became more pronounced when increasing the content of Pd. It is likely because of the oxidation of Pd during the calcination in air. Note that, the Pd 3 d and Au 4 d overlapped and it is difficult to estimate the oxidized Pd content [41]. $Au_{0.07}Pd_{0.93}$-5@NC show more metallic Au(0) with a lower binding energy, compared to other catalysts, given that Pd has a lower oxidation potential than Au (Fig. 5b).

The change in nanostructures of bimetallic NPs before and after calcination was further revealed using HAADF-STEM. Since the initial Au seeds are less than 2 nm, it is very challenging to analyze the crystal lattices of the core and the shell directly using electron microscopy. The dark-field STEM images were recorded using $Au_{0.07}Pd_{0.93}$-5@NC because the pure Pd shell should have the better contrast with Au seeds. NPs grown on the nitrided carbon support did not aggregate or sinter after calcination (Fig. 6). The average size is measured to be about 4.9 ± 0.4 nm. The dark-field STEM images of as-prepared $Au_{0.07}Pd_{0.93}$-5@NC exhibit larger contrast where a brighter core is surrounded by a relatively darker shell (as circled in Fig. 6c). This contrast is likely because of the electron density difference of the core (Au) and the shell (Pd). In contrast, after calcination the boundary between the Au core and Pd shell blurred and even disappeared on most of NPs, suggesting that the diffusion of the core and the shell to form more uniform alloyed NPs.

The catalytic activity of Au_xPd_{1-x}@NC for the electrochemical ethanol oxidation was examined using CV in N_2-saturated 1 M NaOH solutions with different concentrations of ethanol at a scan rate of 50 mV/s. All the currents were normalized to both the

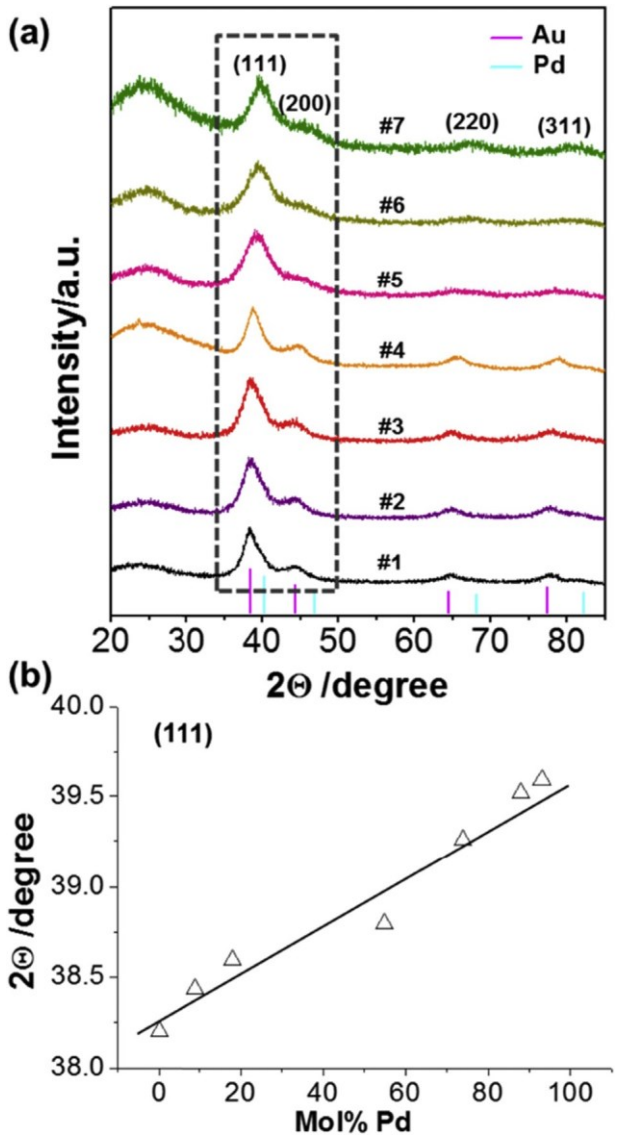

Fig. 3. (a) XRD patterns and (b) (111) diffraction peak positions for (#1) Au-5@NC, (#2) $Au_{0.91}Pd_{0.09}$-5@NC, (#3) $Au_{0.82}Pd_{0.18}$-5@NC, (#4) $Au_{0.45}Pd_{0.55}$-5@NC, (#5) $Au_{0.26}Pd_{0.74}$-5@NC, (#6) $Au_{0.12}Pd_{0.88}$-5@NC and (#7) $Au_{0.07}Pd_{0.93}$-5@NC.

loading mass and the ECSAs of metals including Au and Pd on the PG electrode. For Au-5@NC, the oxidation peak current at ~0.11 V in

Table 2
The electrochemical active surface area (ECSA) and the fitted equivalent circuit parameters of ethanol oxidation for materials with the varying ratios of Au/Pd.

Samples	ECSA (cm^2)	C_{dl} (mF)	R_{ct} (Ω)	k^0 (cm/s)
Au-5@NC	1.41	0.12	54.6	2.5×10^{-6}
$Au_{0.91}Pd_{0.09}$-5@NC	3.37	0.39	66.3	2.1×10^{-6}
$Au_{0.82}Pd_{0.18}$-5@NC	2.68	0.19	27.1	5.0×10^{-6}
$Au_{0.45}Pd_{0.55}$-5@NC	3.09	0.90	21.2	6.4×10^{-6}
$Au_{0.26}Pd_{0.74}$-5@NC	4.72	0.26	25.2	5.4×10^{-6}
$Au_{0.12}Pd_{0.88}$-5@NC	6.83	1.22	36.9	3.7×10^{-6}
$Au_{0.07}Pd_{0.93}$-5@NC	2.66	0.16	21.7	6.2×10^{-6}
5% Pd/C	1.30	0.54	42.0	3.2×10^{-6}

the anodic scans increased with the concentration of ethanol (Fig. 7a). The mass activity, known as the mass-normalized peak current density, increased up to 0.14 $A/mg_{Au\&Pd}$ in 0.6 M ethanol. The peak current started to level off when the concentration of ethanol is higher than 0.6 M (Fig. 7b). This is mostly contributed by the limited active sites on the surface of the electrode [37,42,43]. At higher ethanol concentration, the oxidation activity cannot increase since all active sites are occupied by the adsorbed ethanol. Fig. 7c shows the CV scans of Au-5@NC in N_2-saturated 1 M NaOH solutions with 0.6 M ethanol at different scan rates up to 150 mV/s. A linear relationship when plotting the catalytic peak current density against the square root of the scan rate ($v^{1/2}$) is seen in Fig. 7d, indicating the diffusion controlled mechanism in the electrochemical ethanol oxidation by Au-5@NC.

The electrocatalytic activity of $Au_{0.07}Pd_{0.93}$-5@NC is showed in Fig. 8. A similar oxidation behavior was observed on AuPd bimetallic NPs. However, a large backward oxidation peak was seen in all cases (see Fig. S5). The proportional increase of oxidation peak current at ca. −0.29 V with the concentration of ethanol (<0.6 M) was also observed. The mass activity peaked at 0.23 $A/mg_{Au\&Pd}$ with 0.6 M ethanol, followed by a plateau when further increasing the concentration of ethanol as shown in Fig. 8b. The maximum mass activity of $Au_{0.07}Pd_{0.93}$-5@NC is ca. 1.6 times higher compared to that of Au-5@NC. The similar diffusion controlled mechanism can also be determined from the linear manner between peak current density and $v^{1/2}$ plotted in the Fig. 8c and d.

Catalytic activities of Au_xPd_{1-x}-5@NC with different compositions toward ethanol oxidation were also evaluated and summarized in Fig. 9. With a higher content of Pd (>50%), Au_xPd_{1-x}-5@NC shows the oxidation peak potentials of ethanol around −0.25 V, that is ca. 360 mV less positive than that of Au-rich catalysts (the Pd content <50%) (see Fig. 9a and b). Pd has been reported as a good catalyst for the alcohol oxidation in alkaline media [44,45]. With a low content of Au (<50%), the low oxidation potentials suggest that the thermodynamic binding affinity of ethanol was not varied on

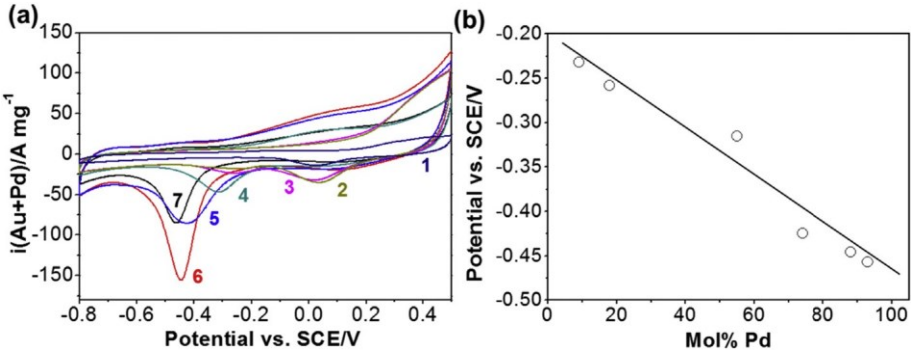

Fig. 4. (a) CVs in N_2-saturated 1 M NaOH at 50 mV/s and (b) Oxygen desorption peak position for (#1) Au-5@NC, (#2) $Au_{0.91}Pd_{0.09}$-5@NC, (#3) $Au_{0.82}Pd_{0.18}$-5@NC, (#4) $Au_{0.45}Pd_{0.55}$-5@NC, (#5) $Au_{0.26}Pd_{0.74}$-5@NC, (#6) $Au_{0.12}Pd_{0.88}$-5@NC and (#7) $Au_{0.07}Pd_{0.93}$-5@NC. All samples were calcined to remove surface ligands.

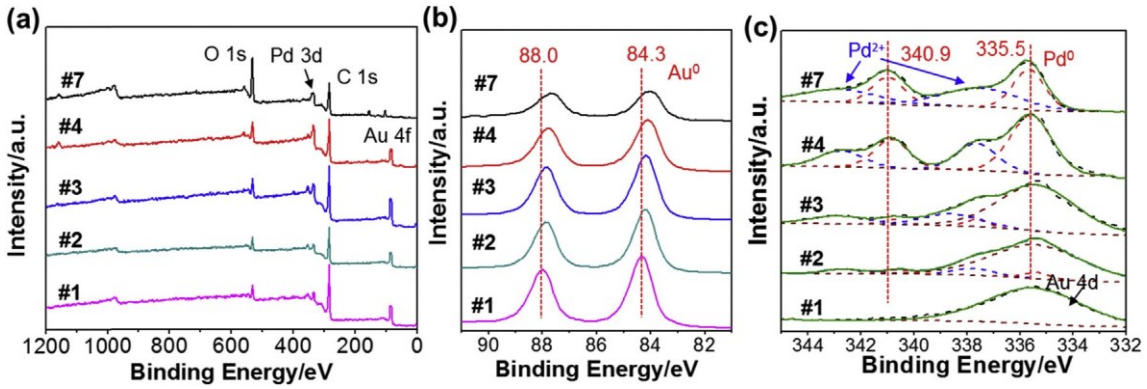

Fig. 5. (a) Survey XPS spectra, high resolution (b) Au 4f and (c) Pd 3 d XPS spectra of (#1) Au-5@NC, (#2) $Au_{0.91}Pd_{0.09}$-5@NC, (#3) $Au_{0.82}Pd_{0.18}$-5@NC, (#4) $Au_{0.45}Pd_{0.55}$-5@NC and (#7) $Au_{0.07}Pd_{0.93}$-5@NC.

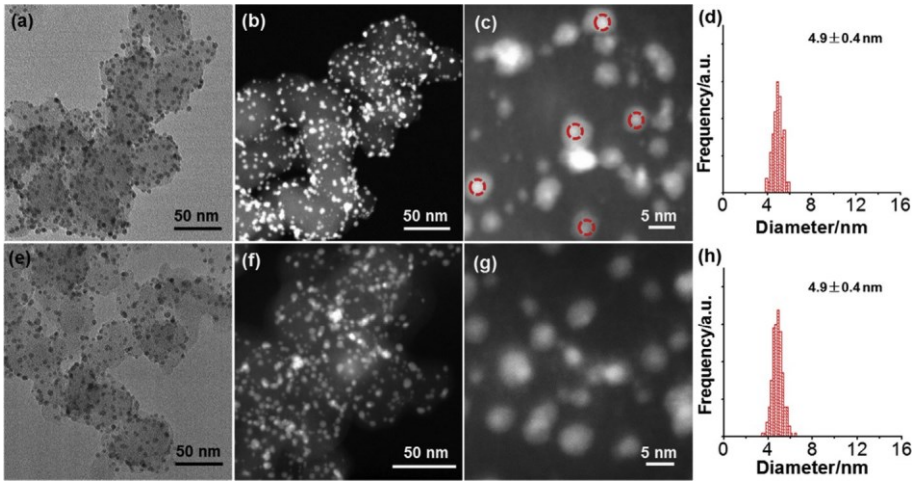

Fig. 6. Respective (a, e) TEM images, (b-c, f-g) HAADF-STEM images and (d, h) the size distribution histograms of $Au_{0.07}Pd_{0.93}$-5@NC before (aed) and after (eeh) calcination. The dark field image in (c) show the core-shell structures as circled.

bimetallic NPs compared to that of pure Pd NPs. However, the mass activity (normalized to the loading mass of metal NPs in the catalysts) and the specific activity of bimetallic NPs (normalized to the ECSAs of the catalysts) are largely improved compared to $Au_{0.07}Pd_{0.93}$-5@NC and commercial Pd black (5 wt% loading). For example, $Au_{0.45}Pd_{0.55}$-5@NC exhibits the highest mass activity (0.43 A/mg_{Au+Pd}) and specific activity (1.11 mA/cm^2) toward ethanol oxidation in comparison with the other catalysts. It is approximately 5 times more active (specific activity) than that of commercial Pd black on carbon (5% Pd/C), and 2.3 times more active than that of $Au_{0.07}Pd_{0.93}$-5@NC, respectively, as summarized in the Fig. 9c. To evaluate the size effect on the electrochemical properties of AuPd bimetallic catalysts, Au_xPd_{1-x}@NC of 2.5 nm and 3.5 nm was prepared for comparison. $Au_{0.70}Pd_{0.30}$-2.5@NC showed the highest specific activity of 4.43 mA/cm^2 toward ethanol oxidation as given in Fig. S6, although the content of bimetallic NPs has a deviation from the feeding ratio due to the presence of Au seeds.

When performing ethanol oxidation, carbonaceous intermediates, e.g. aldehydes and acids, form first in the anodic scan; and then the adsorbed intermediates are further oxidized to desorb those intermediates in the backward sweep. Thus, the peak associated with the removal of incompletely oxidized carbonaceous species was observed in the reserve scan (Fig. S7). Thus, the activity ratio of the forward scan (j_f) to the backward scan (j_b) peaks, j_f/j_b, represents the accumulation of carbonaceous intermediates on the electrode. The j_f/j_b was plotted in Fig. 9d. The highest j_f/j_b ratio of $Au_{0.91}Pd_{0.09}$-5@NC was 5.8 among all catalysts. This value was even higher than that of Au-5@NC, which showed the weak binding to CO and other species as studied in our previous report [37]. It is mainly attributed to the synergic effect between Au and Pd; that is, Pd contributes to the enhanced activity and the neighbor Au helps to desorb the accumulated intermediates. While, the j_f/j_b ratio of $Au_{0.82}Pd_{0.18}$-5@NC decreased dramatically to 2.5 with a bit higher Pd concentration. Other catalysts having higher Pd content gave a much lower j_f/j_b ratio of 0.5e0.6, indicating that the more Pd fraction on the surface of NPs resulted in the accumulation of carbonaceous intermediates and inhibited the catalytic activity.

CO is often considered as the main poisoning intermediates in DAFCs on Pd-based catalysts [44,46e48]. We used CO stripping voltammetry to ascertain the effect of the AuPd alloys on the enhanced catalytic stability against CO poisoning. The CO stripping voltammetry was recorded at a sweep rate of 50 mV/s in the potential window of 0e1.3 V. A very broad oxidation peak from 0.6 to 1.1 V appeared in the first cycle for all the catalysts except the pure Au-5@NC and $Au_{0.91}Pd_{0.09}$-5@NC which is assigned to the oxidation of surface adsorbed CO molecules (Fig. 10). This was confirmed by performing the second scan where the oxidation peak disappeared. All bimetallic NPs containing highly than >10% of Pd are subjected to CO poisoning. The superior CO-tolerance performance of Au-5@NC and $Au_{0.91}Pd_{0.09}$-5@NC was seen likely because of weak

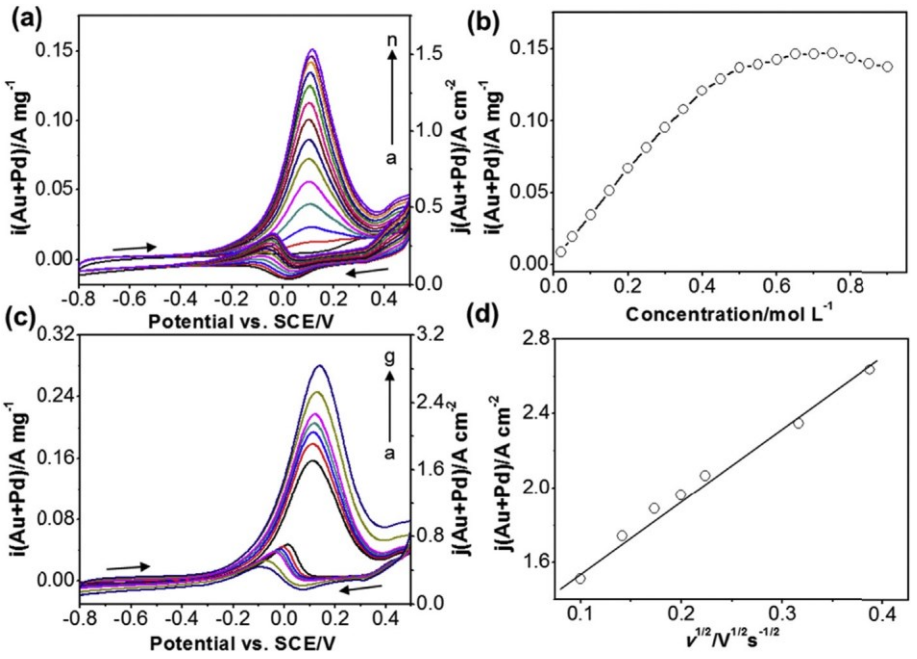

Fig. 7. (a) CVs for Au-5@NC after calcination at 50 mV/s in N_2 saturated 1 M NaOH containing (a) 0, (b) 0.02, (c) 0.05, (d) 0.10, (e) 0.15, (f) 0.20, (g) 0.25, (h) 0.30, (i) 0.35, (j) 0.40, (k) 0.45, (l) 0.50, (m) 0.55, and (n) 0.60 M ethanol. (b) Dependence of CV oxidation peak current density (j) on concentration of ethanol. (c) CVs of 0.6 M ethanol in N_2 saturated 1 M NaOH solution for Au-5@NC at different scan rates (mV/s): (a) 10, (b) 20, (c) 30, (d) 40, (e) 50, (f) 100 and (g) 150. (d) Effect of scan rate (v) on electrocatalytic oxidation peak current density of ethanol for Au-5@NC.

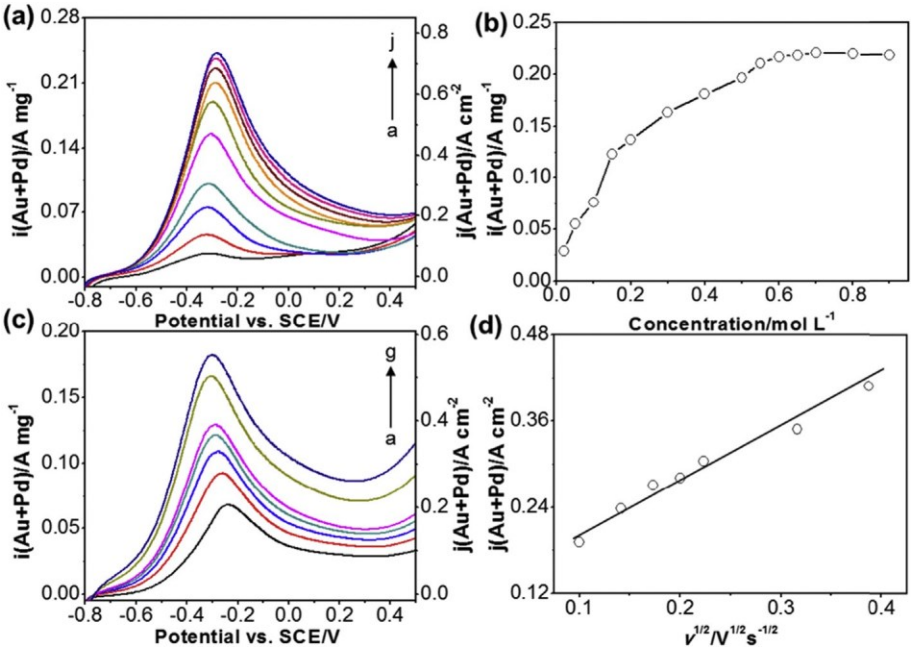

Fig. 8. (a) The forward scans of CVs for $Au_{0.07}Pd_{0.93}$-5@NC after calcination at 50 mV/s in N_2 saturated 1 M NaOH containing (a) 0, (b) 0.02, (c) 0.05, (d) 0.10, (e) 0.20, (f) 0.30, (g) 0.40, (h) 0.50, (i) 0.55, and (j) 0.60 M ethanol. (b) Dependence of CV oxidation peak current density (j) on concentration of ethanol. (c) The forward scans of CVs of 0.6 M ethanol in N_2 saturated 1 M NaOH solution for $Au_{0.07}Pd_{0.93}$-5@NC at different scan rates (mV/s): (a) 10, (b) 20, (c) 30, (d) 40, (e) 50, (f) 100 and (g) 150. (d) Effect of scan rate (v) on electrocatalytic oxidation peak current density of ethanol for $Au_{0.07}Pd_{0.93}$-5@NC.

binding affinity to CO. Those results are consistent with the larger j_f/j_b ratios for Au-5@NC and $Au_{0.91}Pd_{0.09}$-5@NC compared to other catalysts (Fig. 9d). There are two CO stripping shoulder peaks for the $Au_{0.91}Pd_{0.09}$-5@NC and $Au_{0.82}Pd_{0.18}$-5@NC. That means there are two different active sites that have different binding affinity to CO molecules in these catalysts. This was also observed in other Pd-rich catalysts [49].

In order to investigate the electrochemical stability of Au_xPd_{1-x}-5@NC with different compositions, chronoamperometric response for those catalysts was recorded at peak potential for 1200 s in 1 M NaOH containing 0.6 M ethanol (Fig. S8). The current decay for Au_xPd_{1-x}-5@NC are much slower than pure commercial 5% Pd/C,

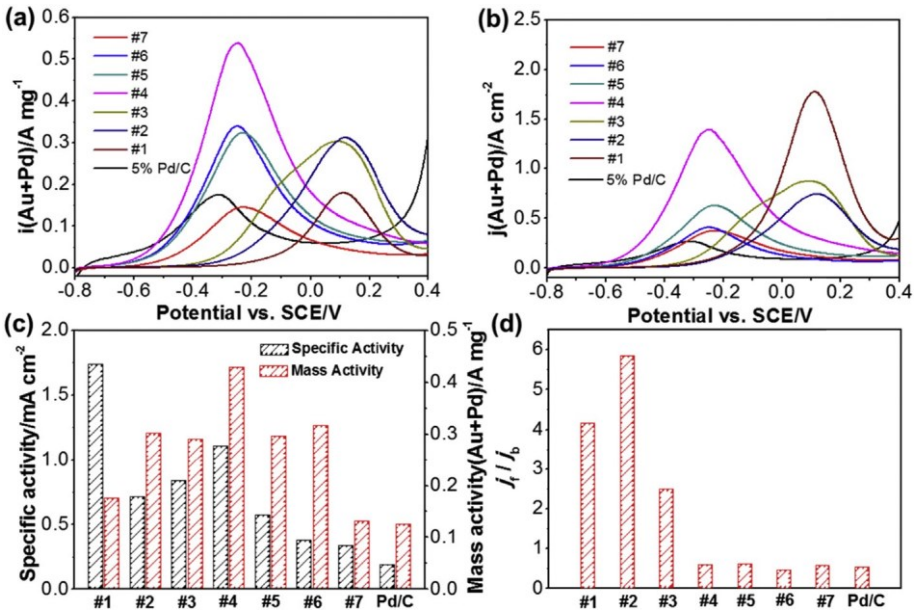

Fig. 9. The current density normalized with respect to the loading mass (a) and the ECSAs (b) in the forward scans for (#1) Au-5@NC, (#2) $Au_{0.91}Pd_{0.09}$-5@NC, (#3) $Au_{0.82}Pd_{0.18}$-5@NC, (#4) $Au_{0.45}Pd_{0.55}$-5@NC, (#5) $Au_{0.26}Pd_{0.74}$-5@NC, (#6) $Au_{0.12}Pd_{0.88}$-5@NC, (#7) $Au_{0.07}Pd_{0.93}$-5@NC and commercial 5% Pd/C loaded on PG electrode. All curves are obtained in 1 M NaOH containing 0.6 M ethanol at 20 mV/s. (c) Comparison of specific and mass activity of Au_xPd_{1-x}-5@NC with different molar ratio. (d) Dependence of CV oxidation peak current density ratio of the forward (j_f) to the backward scan (j_b), j_f/j_b, on the mole fraction of Pd.

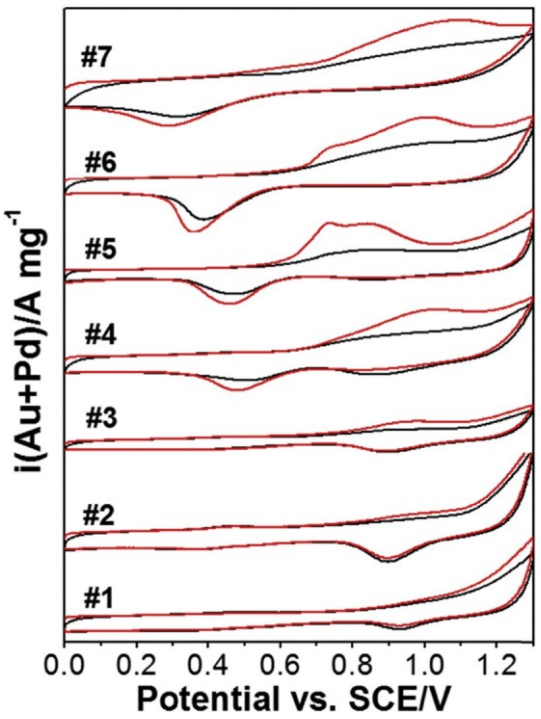

Fig. 10. CO stripping voltammetry (red: first cycle, black: second cycle) for (#1) Au-5@NC, (#2) $Au_{0.91}Pd_{0.09}$-5@NC, (#3) $Au_{0.82}Pd_{0.18}$-5@NC, (#4) $Au_{0.45}Pd_{0.55}$-5@NC, (#5) $Au_{0.26}Pd_{0.74}$-5@NC, (#6) $Au_{0.12}Pd_{0.88}$-5@NC and (#7) $Au_{0.07}Pd_{0.93}$-5@NC in 0.5 M H_2SO_4 at 50 mV/s. (For interpretation of the references to colour in this figure legend, the reader is referred to the Web version of this article.)

indicating that alloying Au with Pd not only enhances the electrocatalytic activity, but also improves the stability of catalysts [25,50,51]. Noticeably, $Au_{0.45}Pd_{0.55}$-5@NC maintained the highest steady-state current density that is ca. 2.9 times higher than that of commercial 5% Pd/C. The enhanced electrochemical stability and the results from CO stripping voltammetry confirm that the presence of Au is beneficial for the removal of adsorbed poisoning species during the continuous electrocatalytic oxidation of ethanol.

As reported previously, ethanol is oxidized to acetate on Pd-based electrocatalysts especially in the strongly alkaline media [52,53]. The overall oxidation of ethanol can be described by eq (1).

$$CH_3CH_2OH + 5OH^- \rightarrow CH_3COO^- + 4H_2O + 4e^- \quad (1)$$

A generally accepted reaction mechanism for ethanol oxidation on Pd-based catalysts in alkaline media involved four consecutive steps (eqs (2)e(5)) [15,44].

$$M + OH^- \rightarrow M-OH_{ads} + e^- \quad (2)$$

$$M-(CH_3CH_2OH)_{ads} + 3OH^- \rightarrow M-(COCH_3)_{ads} + 3H_2O + 3e^- \quad (3)$$

$$M-(COCH_3)_{ads} + M-OH_{ads} \rightarrow M-CH_3COOH + M \quad (4)$$

$$M-CH_3COOH + OH^- \rightarrow M + CH_3COO^- + H_2O \quad (5)$$

The rate determining step is the stripping of the adsorbed ethoxi species. Therefore, the weak binding to CO_{ads} on the bimetallic NPs of AuPd will accelerate the removal of the ethoxi intermediates, reduce the charge transfer resistance and result in the enhancement in the reaction kinetics. Electrochemical impedance spectra (EIS) were used to further study the charge transfer kinetics. Fig. 11a and Fig. S9 display the EIS of all catalysts obtained at peak potential in the frequency range of 0.1e100000 Hz. The EIS spectra can allow us to better understand the interfacial process and reaction kinetics in this system. The charge transfer resistance (R_{ct}) and the rate constant (k^0) estimated from the equivalent circuit fit curves are given in Table 2 [54,55]. The pure Au-5@NC and Au-rich catalysts show large impedance arcs in the Nyquist plot and have charge transfer resistances of 54.6 and 66.3 Ω, respectively. Those are 2e3

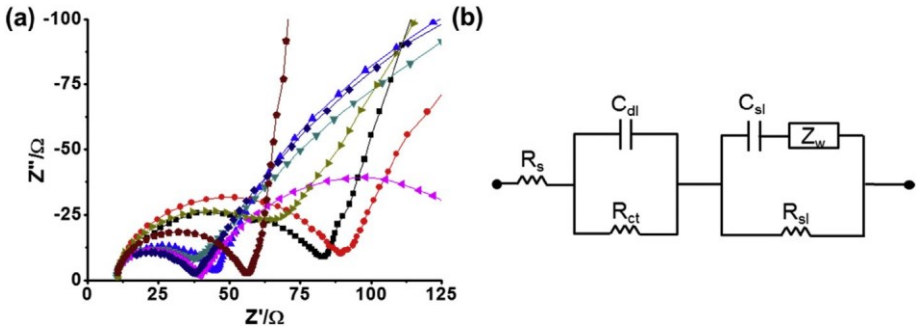

Fig. 11. (a) Electrochemical impedance spectra for (#1) Au-5@NC, (#2) $Au_{0.91}Pd_{0.09}$-5@NC, (#3) $Au_{0.82}Pd_{0.18}$-5@NC, (#4) $Au_{0.45}Pd_{0.55}$-5@NC, (#5) $Au_{0.26}Pd_{0.74}$-5@NC, (#6) $Au_{0.12}Pd_{0.88}$-5@NC, (#7) $Au_{0.07}Pd_{0.93}$-5@NC and commercial 5% Pd/C in N_2 saturated 1 M NaOH containing 0.6 M ethanol at peak potential. (b) The best fit equivalent circuit model for the complex impedance. R_s, is solution resistance, R_{ct}, is charge transfer resistance and R_{sl}, is resistance to migration respectively, while C_{dl}, is electric double layer capacitance of the electrode, C_{sl}, is capacitance of the surface passivation layer, and Z_w, is Warburg impedance.

times higher than that of other bimetallic catalysts. After incorporating Pd to Au, the higher conductivity and acceleration of charge transfer was obtained, evident with the smaller R_{ct} between 21.2 and 36.9 Ω. The k^0 of $Au_{0.45}Pd_{0.55}$-5@NC is 6.4 × 10^{-6} cm/s that is 3-folder higher than that of pure Au and $Au_{0.91}Pd_{0.09}$-5@NC. This further proves the AuPd alloy have faster electrolysis rates for the ethanol oxidation [37].

4. Conclusions

In summary, we demonstrated the direct growth of well-defined AuPd bimetallic NPs in the size range of 2e5 nm on nitrided carbon support. Our method is based on a seed-mediated growth and it provides a promising way to precisely tune the sizes and chemical compositions of bimetallic NPs. Ultrasmall Au nanocrystals supported on nitrided carbon were used as seeds to grow AuPd bimetallic shells. We showed the mass loading of AuPd bimetallic NPs on carbon supports reached 40 wt% without any aggregation. The resultant core-shell AuPd bimetallic NPs were thermally stable and could be converted to AuPd alloyed NPs when subjected to thermal annealing at 250 °C for 1 h. The chemical compositions of the AuPd alloyed NPs were investigated by combining SEM-EDX mapping, XPS and surface oxygen desorption using electrochemical reduction of catalysts. The catalytic activity, stability, poisoning tolerance and electrical conductivity in the ethanol electrooxidation relative to the monometallic catalysts can be largely enhanced by the incorporation of Au into Pd. $Au_{0.45}Pd_{0.55}$-5@NC exhibited superior mass activity (0.43 A/mg_{AuPd}) and specific activity (1.11 mA/cm^2) toward ethanol oxidation in comparison with the other catalysts, approximately 5 times more active than commercial 5% Pd/C and maintained the highest steady-state current density after 1200 s that is ca. 2.9 times higher than that of commercial 5% Pd/C. We expect that this synthetic method will be of interest to prepare electrocatalysts having defined nanostructures and compositions directly on conductive carbon for applications in fuel cells and batteries.

Acknowledgements

This research was supported in part by the National Science Foundation (CBET 1705566). Y.Y. thanks the support from the China Scholarship Council and Nanjing University of Science and Technology for her visiting at the University of Connecticut. The SEM/TEM studies were performed using the facilities in the UConn/FEI Center for Advanced Microscopy and Materials Analysis (CAMMA). This work was also partially supported by the Green Emulsions Micelles and Surfactants (GEMS) Center.

Appendix A. Supplementary data

Supplementary data related to this article can be found at https://doi.org/10.1016/j.electacta.2018.03.017.

References

[1] C.K. Dyer, Fuel cells for portable applications, Fuel Cells Bull. 2002 (2002) 8e9.
[2] E. Antolini, Catalysts for direct ethanol fuel cells, J. Power Sources 170 (2007) 1e12.
[3] C. Lamy, A. Lima, V. LeRhun, F. Delime, C. Coutanceau, J.-M. Lĕger, Recent advances in the development of direct alcohol fuel cells (DAFC), J. Power Sources 105 (2002) 283e296.
[4] R. Dillon, S. Srinivasan, A. Arico, V. Antonucci, International activities in DMFC R&D: status of technologies and potential applications, J. Power Sources 127 (2004) 112e126.
[5] H.R. Corti, E.R. Gonzalez, Direct Alcohol Fuel Cells: Materials, Performance, Durability and Applications, Springer Science & Business Media, 2013.
[6] M. Kamarudin, S.K. Kamarudin, M. Masdar, W.R.W. Daud, Direct ethanol fuel cells, Int. J. Hydrog. Energy 38 (2013) 9438e9453.
[7] J.-H. Wee, K.-Y. Lee, Overview of the development of CO-tolerant anode electrocatalysts for proton-exchange membrane fuel cells, J. Power Sources 157 (2006) 128e135.
[8] K. Ding, Y. Zhao, L. Liu, Y. Cao, Q. Wang, H. Gu, X. Yan, Z. Guo, PteNi bimetallic composite nanocatalysts prepared by using multi-walled carbon nanotubes as reductants for ethanol oxidation reaction, Int. J. Hydrog. Energy 39 (2014) 17622e17633.
[9] T. Lopes, E. Antolini, F. Colmati, E.R. Gonzalez, Carbon supported PteCo (3: 1) alloy as improved cathode electrocatalyst for direct ethanol fuel cells, J. Power Sources 164 (2007) 111e114.
[10] C.-T. Hsieh, J.-Y. Lin, Fabrication of bimetallic PteM (M¼ Fe, Co, and Ni) nanoparticle/carbon nanotube electrocatalysts for direct methanol fuel cells, J. Power Sources 188 (2009) 347e352.
[11] W. Li, W. Zhou, H. Li, Z. Zhou, B. Zhou, G. Sun, Q. Xin, Nano-structured PteFe/C as cathode catalyst in direct methanol fuel cell, Electrochim. Acta 49 (2004) 1045e1055.
[12] Z. Liu, G.S. Jackson, B.W. Eichhorn, PtSn intermetallic, coreeshell, and alloy nanoparticles as CO-tolerant electrocatalysts for H2 oxidation, Angew. Chem. Int. Ed. 49 (2010) 3173e3176.
[13] L. Dong, R.R.S. Gari, Z. Li, M.M. Craig, S. Hou, Graphene-supported platinum and platinumeruthenium nanoparticles with high electrocatalytic activity for methanol and ethanol oxidation, Carbon 48 (2010) 781e787.
[14] S. Zhou, K. McIlwrath, G. Jackson, B. Eichhorn, Enhanced CO tolerance for hydrogen activation in Au– Pt dendritic heteroaggregate nanostructures, J. Am. Chem. Soc. 128 (2006) 1780e1781.
[15] C. Bianchini, P.K. Shen, Palladium-based electrocatalysts for alcohol oxidation in half cells and in direct alcohol fuel cells, Chem. Rev. 109 (2009) 4183e4206.
[16] Z.-L. Wang, J.-M. Yan, H.-L. Wang, Y. Ping, Q. Jiang, Au@ Pd coreeshell nanoclusters growing on nitrogen-doped mildly reduced graphene oxide with enhanced catalytic performance for hydrogen generation from formic acid, J. Mater. Chem. A 1 (2013) 12721e12725.
[17] L.-X. Chen, L.-Y. Jiang, A.-J. Wang, Q.-Y. Chen, J.-J. Feng, Simple synthesis of bimetallic AuPd dendritic alloyed nanocrystals with enhanced electrocatalytic performance for hydrazine oxidation reaction, Electrochim. Acta 190 (2016) 872e878.
[18] K.D. Gilroy, A. Ruditskiy, H.-C. Peng, D. Qin, Y. Xia, Bimetallic nanocrystals: syntheses, properties, and applications, Chem. Rev. 116 (2016) 10414e10472.
[19] J.-J. Lv, S.-S. Li, A.-J. Wang, L.-P. Mei, J.-R. Chen, J.-J. Feng, Monodisperse Au-Pd bimetallic alloyed nanoparticles supported on reduced graphene oxide with enhanced electrocatalytic activity towards oxygen reduction reaction,

Electrochim. Acta 136 (2014) 521e528.
[20] J.-M. Léger, S. Rousseau, C. Coutanceau, F. Hahn, C. Lamy, How bimetallic electrocatalysts does work for reactions involved in fuel cells?: example of ethanol oxidation and comparison to methanol, Electrochim. Acta 50 (2005) 5118e5125.
[21] C. Zhu, S. Guo, S. Dong, PdM (M¼ Pt, Au) bimetallic alloy nanowires with enhanced electrocatalytic activity for electro-oxidation of small molecules, Adv. Mater. 24 (2012) 2326e2331.
[22] Y.-Y. Feng, Z.-H. Liu, Y. Xu, P. Wang, W.-H. Wang, D.-S. Kong, Highly active PdAu alloy catalysts for ethanol electro-oxidation, J. Power Sources 232 (2013) 99e105.
[23] C. Xu, Z. Tian, Z. Chen, S.P. Jiang, Pd/C promoted by Au for 2-propanol electrooxidation in alkaline media, Electrochem. Commun. 10 (2008) 246e249.
[24] L. Zhu, T. Zhao, J. Xu, Z. Liang, Preparation and characterization of carbon-supported sub-monolayer palladium decorated gold nanoparticles for the electro-oxidation of ethanol in alkaline media, J. Power Sources 187 (2009) 80e84.
[25] F. Ksar, L. Ramos, B. Keita, L. Nadjo, P. Beaunier, H. Remita, Bimetallic palladium– gold nanostructures: application in ethanol oxidation, Chem. Mater. 21 (2009) 3677e3683.
[26] L. Wang, Y. Nemoto, Y. Yamauchi, Direct synthesis of spatially-controlled Pt-on-Pd bimetallic nanodendrites with superior electrocatalytic activity, J. Am. Chem. Soc. 133 (2011) 9674e9677.
[27] K. Esumi, T. Tano, K. Torigoe, K. Meguro, Preparation and characterization of bimetallic palladium-copper colloids by thermal decomposition of their acetate compounds in organic solvents, Chem. Mater. 2 (1990) 564e567.
[28] M. Cargnello, C. Chen, B.T. Diroll, V.V. Doan-Nguyen, R.J. Gorte, C.B. Murray, Efficient removal of organic ligands from supported nanocrystals by fast thermal annealing enables catalytic studies on well-defined active phases, J. Am. Chem. Soc. 137 (2015) 6906e6911.
[29] B. Liu, H. Yao, W. Song, L. Jin, I.M. Mosa, J.F. Rusling, S.L. Suib, J. He, Ligand-free noble metal nanocluster catalysts on carbon supports via "soft" nitriding, J. Am. Chem. Soc. 138 (2016) 4718e4721.
[30] J. He, Y. Wang, Z. Fan, Z. Lam, H. Zhang, B. Liu, H. Chen, Substrate-bound growth of AuePd diblock nanowire and hybrid nanorodeplate, Nanoscale 7 (2015) 8115e8121.
[31] J.A. Lopez-Sanchez, N. Dimitratos, C. Hammond, G.L. Brett, L. Kesavan, S. White, P. Miedziak, R. Tiruvalam, R.L. Jenkins, A.F. Carley, D. Knight, C.J. Kiely, G.J. Hutchings, Facile removal of stabilizer-ligands from supported gold nanoparticles, Nat. Chem. 3 (2011) 551.
[32] G. Ma, A. Binder, M. Chi, C. Liu, R. Jin, D.-e. Jiang, J. Fan, S. Dai, Stabilizing gold clusters by heterostructured transition-metal oxideemesoporous silica supports for enhanced catalytic activities for CO oxidation, Chem. Commun. 48 (2012) 11413e11415.
[33] R. Woods, In Electroanalytical Chemistry: a Series of Advances, Marcel Dekker, New York, 1974.
[34] B. Liu, P. Wang, A. Lopes, L. Jin, W. Zhong, Y. Pei, S.L. Suib, J. He, AueCarbon electronic interaction mediated selective oxidation of styrene, ACS Catal. 7 (2017) 3483e3488.
[35] J.S. Jirkovsky, I. Panas, E. Ahlberg, M. Halasa, S. Romani, D.J. Schiffrin, Single atom hot-spots at AuePd nanoalloys for electrocatalytic H_2O_2 production, J. Am. Chem. Soc. 133 (2011) 19432e19441.
[36] Y.W. Lee, M. Kim, Y. Kim, S.W. Kang, J.-H. Lee, S.W. Han, Synthesis and electrocatalytic activity of Au–Pd alloy nanodendrites for ethanol oxidation, J. Phys. Chem. C 114 (2010) 7689e7693.
[37] H. Yao, B. Liu, I.M. Mosa, I. Bist, J. He, J.F. Rusling, Electrocatalytic oxidation of alcohols, tripropylamine, and DNA with ligand-free gold nanoclusters on nitrided carbon, ChemElectroChem 3 (2016) 2100e2109.
[38] L. Jin, B. Liu, S.S. Duay, J. He, Engineering surface ligands of noble metal nanocatalysts in tuning the product selectivity, Catalysts 7 (2017) 44.
[39] R. Woods, Electrochim. Acta 14 (1969).
[40] D.A.J.R.a.R. Woods, J. Electroanal. Chem. 36 (1972).
[41] C. Bi, C. Feng, T. Miao, Y. Song, D. Wang, H. Xia, Understanding the effect of ultrathin AuPd alloy shells of irregularly shaped Au@ AuPd nanoparticles with high-index facets on enhanced performance of ethanol oxidation, Nanoscale 7 (2015) 20105e20116.
[42] S. Yan, S. Zhang, Y. Lin, G. Liu, Electrocatalytic performance of gold nanoparticles supported on activated carbon for methanol oxidation in alkaline solution, J. Phys. Chem. C 115 (2011) 6986e6993.
[43] G. Camara, T. Iwasita, Parallel pathways of ethanol oxidation: the effect of ethanol concentration, J. Electroanal. Chem. 578 (2005) 315e321.
[44] Z. Liang, T. Zhao, J. Xu, L. Zhu, Mechanism study of the ethanol oxidation reaction on palladium in alkaline media, Electrochim. Acta 54 (2009) 2203e2208.
[45] L. Ma, D. Chu, R. Chen, Comparison of ethanol electro-oxidation on Pt/C and Pd/C catalysts in alkaline media, Int. J. Hydrog. Energy 37 (2012) 11185e11194.
[46] J.S. Spendelow, A. Wieckowski, Electrocatalysis of oxygen reduction and small alcohol oxidation in alkaline media, Phys. Chem. Chem. Phys. 9 (2007) 2654e2675.
[47] V. Bambagioni, C. Bianchini, A. Marchionni, J. Filippi, F. Vizza, J. Teddy, P. Serp, M. Zhiani, Pd and PteRu anode electrocatalysts supported on multi-walled carbon nanotubes and their use in passive and active direct alcohol fuel cells with an anion-exchange membrane (alcohol¼ methanol, ethanol, glycerol), J. Power Sources 190 (2009) 241e251.
[48] C. Xu, H. Wang, P.K. Shen, S.P. Jiang, Highly ordered Pd nanowire arrays as effective electrocatalysts for ethanol oxidation in direct alcohol fuel cells, Adv. Mater. 19 (2007) 4256e4259.
[49] M. Koper, N. Lebedeva, C. Hermse, Dynamics of CO at the solid/liquid interface studied by modeling and simulation of CO electro-oxidation on Pt and PtRu electrodes, Faraday Disc. 121 (2002) 301e311.
[50] Y.W. Lee, M. Kim, Y. Kim, S.W. Kang, J.-H. Lee, S.W. Han, Synthesis and electrocatalytic activity of Au– Pd alloy nanodendrites for ethanol oxidation, J. Phys. Chem. C 114 (2010) 7689e7693.
[51] J. Xu, T. Zhao, S. Shen, Y. Li, Stabilization of the palladium electrocatalyst with alloyed gold for ethanol oxidation, Int. J. Hydrog. Energy 35 (2010) 6490e6500.
[52] A. Marchionni, M. Bevilacqua, C. Bianchini, Y.X. Chen, J. Filippi, P. Fornasiero, A. Lavacchi, H. Miller, L. Wang, F. Vizza, Electrooxidation of ethylene glycol and glycerol on Pd-(Ni-Zn)/C anodes in direct alcohol fuel cells, ChemSusChem 6 (2013) 518e528.
[53] S. Shen, T. Zhao, Q. Wu, Product analysis of the ethanol oxidation reaction on palladium-based catalysts in an anion-exchange membrane fuel cell environment, Int. J. Hydrog. Energy 37 (2012) 575e582.
[54] R.E. Melnick, G.T.R. Palmore, Impedance spectroscopy of the electro-oxidation of methanol on polished polycrystalline platinum, J. Phys. Chem. B 105 (2001) 1012e1025.
[55] H.T. Zheng, Y. Li, S. Chen, P.K. Shen, Effect of support on the activity of Pd electrocatalyst for ethanol oxidation, J. Power Sources 163 (2006) 371e375.